Heliyon 9 (2023) e17947

Contents lists available at ScienceDirect

Heliyon

journal homepage: www.cell.com/heliyon

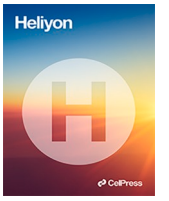

Sulfur deficiency mediated visible emission of ZnS QDs by magnesium dopant and their application in waste water treatment

S. Murugan [a], M. Ashokkumar [a,*], P. Sakthivel [b], Dongjin Choi [c,**]

[a] Department of Physics, Saveetha School of Engineering, Saveetha Institute of Medical and Technical Sciences, Saveetha University, Thandalam, Chennai - 602 105, India

[b] Centre for Materials Science, Department of Physics, Faculty of Engineering, Karpagam Academy of Higher Education, Coimbatore - 641 021, Tamil Nadu, India

[c] Department of Materials Science and Engineering, Hongik University, 2639-Sejong-ro,Jochiwon-eup, Sejong-city, 30016, South Korea

ARTICLE INFO

Keywords:
Zinc sulfide
Magnesium dopant
Antibacterial activity
Photocatalytic activity
Photoluminescence

ABSTRACT

The photocatalyst with antimicrobial activity serves as a better candidate material for wastewater treatment, as wastewater contains microbes, hazardous dyes, and heavy metals. Hence, the present study extensively examines the photocatalytic and antibacterial activities against two waterborne bacterial strains, namely *Salmonella typhi* and *Escherichia coli*. Pure and Mg-doped ZnS (Mg:ZnS) quantum dots (QDs) were synthesized using a low-cost and simple co-precipitation method. The QDs' structural, surface morphology, chemical purity, and optical characteristics were analyzed through XRD, SEM, EDAX, TEM, UV–visible, and photoluminescence spectra. The incorporation of Mg dopants did not introduce significant alterations to the cubic blende structure of ZnS, nor did it induce substantial changes in the structural parameters. However, the QDs exhibited a slight sulfur deficiency, which was further increased by the presence of Mg dopant. The Mg dopant, due to its dominant compositional effect, reduced the band gap. Several optical emission bands were observed in the UV, violet, blue, and green regions, corresponding to NBE emission, sulfur-related defects, and Zn-related defects. Initially, Mg doping enhanced visible emission related to defects, while NBE emission was suppressed by the Mg dopant. However, increasing the concentration of the Mg dopant led to a slight increase in NBE emission. The Mg dopant enhanced the photocatalytic activity of the QDs, and a strong correlation was found between photocatalytic activity and NBE emission. The presence of the Mg dopant led to an increased rate of ROS-based decolorization by reducing the electron-hole recombination rate.

1. Introduction

In recent years, the management of wastewater has emerged as a significant environmental concern, driven by factors such as population growth and the increasing presence of industrial pollutants [1]. Among these pollutants, effluents from dye industries are particularly hazardous, as they are often non-biodegradable and pose significant risks to ecosystems and human health [2]. Methyl orange, a colored dye commonly used in textile, photography paper, and printer industries, is of particular concern [3,4]. To address this issue, catalysts with the ability to utilize sunlight for the eradication of harmful pathogens and pollutants have gained significant

* Corresponding author.
** Corresponding author.
E-mail addresses: ashokphy16@gmail.com (M. Ashokkumar), djchoi@honigk.ac.kr (D. Choi).

https://doi.org/10.1016/j.heliyon.2023.e17947
Received 30 March 2023; Received in revised form 28 June 2023; Accepted 3 July 2023
Available online 11 July 2023

attention as a promising solution for wastewater treatment [5,6]. Metallic semiconductors, in particular, have been extensively employed due to their low toxicity, high oxidation potential, ease of synthesis, and other advantageous properties, enabling the breakdown of organic contaminants in wastewater [7]. Photocatalysts, chosen based on their band gaps, have been identified as suitable candidates for ultraviolet or visible light-driven photocatalysis [8,9]. The process of photocatalysis involves three sequential steps: absorption of photons from sunlight, generation of electron and hole pairs, and surface reactions on the photocatalyst governed by the energy levels of electrons and holes in the conduction and valence bands. Enhancing these three steps will consequently elevate the photocatalytic activity [10–12].

Zinc sulfide (ZnS) is a fascinating metallic chalcogenide that possesses remarkable properties, such as high electrical mobility, thermal stability, cost-effectiveness, non-toxicity, and insolubility in water. These characteristics contribute to its wide appeal and potential applications. As a direct bandgap semiconductor, ZnS exhibits excellent photocarrier generation efficiency [13–15]. ZnS functions as an n-type semiconductor photocatalyst and exhibits exceptional chemical stability against hydrolysis and oxidation. With its wide bandgap of 3.68 eV and suitable redox potentials of the conduction band (1.36 eV) and valence band (+2.35 eV), ZnS is highly suitable for various photocatalytic applications [16–20]. Quantum dots (QDs) can be utilized to enhance ZnS photocatalysis, overcoming the challenge of efficient solar light harvesting and further enhancing its light-induced reactivity. ZnS, as a prominent II-IV semiconductor, finds application in various fields such as luminescence, electroluminescence, probes, phosphor coating, pharmaceuticals, Light Emitting Diodes (LEDs), seeds germinations, and non-linear optoelectronic devices [21,22].

Recent research has focused on magnesium-doped ZnO semiconductor photocatalyst materials due to their unique UV absorption and luminescent properties [23–25]. However, the complexity, cost, and use of hazardous gases necessitate the exploration of simpler and more cost-effective synthesis methods for generating size-controlled nanoparticles with minimal contaminants. Among the various synthesis approaches, chemical co-precipitation is preferred due to its simplicity, excellent doping capability, low impurity levels, and high yield [26,27]. While several studies have examined the influence of magnesium doping on the physical characteristics of , there is currently no evidence linking the biological and physical activities. Hence, this present study extensively explores the morphological, optical, antibacterial, and photocatalytic characteristics of nanoparticles composed of magnesium-doped ZnS.

2. Materials and methods

2.1. Materials

For the synthesis of pure and Mg-doped ZnS (Mg:ZnS) quantum dots (QDs), high-purity chemicals (>99% purity) purchased from Merck, including $Zn(CH_3COO)_2{\cdot}2H_2O$, Na_2S, $Mg(CH_3COO)_2{\cdot}2H_2O$ and NH_3, were utilized.

2.2. Synthesis of $Zn_{1-x}Mg_xS$ QDs

The synthesis of pure ZnS QDs and magnesium-doped ZnS (Mg:ZnS) QDs was carried out using the co-precipitation method in this study. Initially, separate solutions of cations and anions were prepared with a concentration of 1 M in 100 ml of deionized water. These solutions were then combined to create the precursor solution for QD synthesis. The cationic solution was continuously stirred at a temperature of 80 °C, and the sodium sulfide solution was gradually introduced into the mixture. Ammonium solution was used to maintain a pH of 9.5 in the reaction mixture. After the reaction, the obtained precipitate was carefully filtered and subjected to multiple washing steps using deionized water and methanol. These washings were performed to eliminate any undesired contaminants that might have formed during the preparation process. The intended doping concentrations of Mg were 0%, 10%, and 20%. Subsequently, the obtained product was dried thoroughly and subjected to annealing at a temperature of 80 °C for a duration of 30 min using a micro-oven. The identical preparation procedure was replicated for all other concentrations, with the resulting samples labelled as ZS1, ZS2, and ZS3 denoting 0%, 10%, and 20% Mg dopant concentrations, respectively.

2.3. Characterization techniques

The crystal structure of both pure ZnS and Mg:ZnS QDs was determined using powder X-ray diffraction (XRD) analysis. XRD patterns were obtained using a RigaKu C/max-2500 diffractometer, equipped with Cu Kα radiation ($\lambda = 1.5406$ Å). The instrument operated at a voltage of 40 kV and a current of 30 mA. Data collection was performed in the 2θ range of 10°–80°. For composition and topological analysis of Zn, S, and Mg elements, energy-dispersive X-ray spectroscopy (EDX) was employed. The analysis was carried out using the K and L lines. The surface morphology of the quantum dots was examined using scanning electron microscopy (SEM) with a JEOL JSM 6390 instrument and high-resolution transmission electron microscopy (HRTEM) with an FEI Technai T20 instrument. X-ray photoelectron spectroscopy (XPS) spectra were recorded using monochromatic Al Kα radiation ($h\nu = 1486.6$ eV) from an X-ray source with the following specifications: spot size of 100 μm, operating power of 25 W, and voltage of 15 kV. High-resolution XPS spectra were collected using a hemispherical analyzer with a pass energy of 23.5 eV, an energy step size of 0.1 eV, and a photoelectron take-off angle of 45° relative to the surface plane. UV–Visible optical absorption studies were conducted to investigate the optical characteristics. The spectral absorption was measured using a UV–Visible spectrometer (Model: lambda 35, Make: Perkin Elmer) with a wavelength range of 300–600 nm. Furthermore, photoluminescence (PL) spectra of the QDs were measured using a fluorescence spectrophotometer (Model: F-2500, Make: Hitachi) with an excitation wavelength of 280 nm.

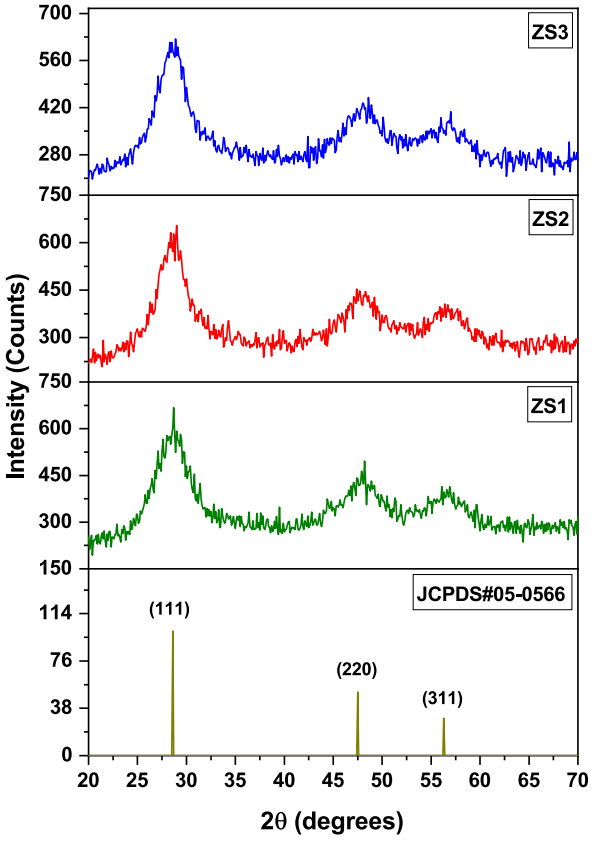

Fig. 1. Powder X-ray diffraction pattern of $Zn_{1-x}Mg_xS$ (x = 0, 0.1 and 0.2) QDs.

2.4. Photocatalytic activity [28]

To evaluate the photocatalytic activity of the samples, an aqueous solution containing methylene blue (MB) with a concentration of 5 mg/L was prepared. A glass culture dish, filled with 10 ml of the MB solution, was positioned near a UV light source with a power of 24 W. The samples, measuring 10 × 10 mm, were fully immersed in the solution, and the distance between the sample and the lamp was maintained at 10 cm. At specific time intervals, the UV–visible absorption of the MB solution was measured using a UV–visible spectrophotometer. The absorbance of the sample at 464 nm was compared with that of the original MB solution to evaluate the photocatalytic activity of the samples.

To assess the reusability of the QDs, the analysis was repeated using the collected QDs after each degradation cycle. The QDs were separated through centrifugation, washed multiple times with double distilled water, and then dried in a vacuum oven at room temperature for 8 h. The collected QDs were used for subsequent photocatalytic analysis, and this series of repeated experiments was referred to as "recycles". Each cycle lasted for 90 min under UV light, and the procedure was repeated for multiple cycles.

In order to gain a deeper understanding of the photocatalytic mechanism of the nanoparticles (NPs), the photocatalytic activity was evaluated in the presence of various scavengers. This allowed for the investigation of the influence of hydrogen peroxide (H_2O_2), hydroxyl radical (OH*), superoxide anions (O_2^-), electrons, and holes on the photocatalytic process.

2.5. Antibacterial assay

For this study, both clinical isolates of microorganisms and standard strains were utilized. The bacterial strains *Salmonella typhi* (MTCCB 733) and *Escherichia coli* (MTCCB 82), used as recommended by the National Committee for Clinical Laboratories Standards (NCCLS), were obtained from the Institute of Microbial Technology in Chandigarh, India. These strains were included in each test conducted.

The antibacterial assay of undoped and Mg-doped ZnS QDs against clinically obtained *Escherichia coli* (*E. Coli*) and *Salmonella typhi* (*S.typhi*) was performed using the agar disc diffusion method. The experimental procedure involved several steps. Initially, a Mueller-Hinton agar medium was meticulously formulated using an autoclave and subjected to sterilization at a temperature of 120 °C for a duration of 30 min. Subsequently, the sterilized medium was carefully moved to a controlled environment to ensure sterility. It was gently poured into sterile petri plates and permitted to solidify under aseptic conditions. Next, the bacterial cultures of *E. Coli* and *S. typhi* were obtained and swabbed onto the surface of each petri plate containing the Mueller-Hinton agar medium. This step ensured

Table 1
The variation of Peak position (2θ), full width at half maximum (FWHM, β) value, d-value, Lattice parameter, Volume and average crystallite size (D) of $Zn_{1-x}Mg_xS$ (x = 0, 0.1 and 0.2) QDs.

Samples	Peak position, 2θ (°)	FWHM, β (degrees)	d-value (Å)	Lattice parameter (Å)	Volume (Å^3)	Average crystallite size, D (nm)
ZnS	28.7	4.4624	3.1243	5.41129	158.454	1.8
$Zn_{0.9}Mg_{0.1}S$	29	3.9875	3.1261	5.41441	158.728	2.0
$Zn_{0.8}Mg_{0.2}S$	28.9	4.2871	3.1253	5.41302	158.606	1.9

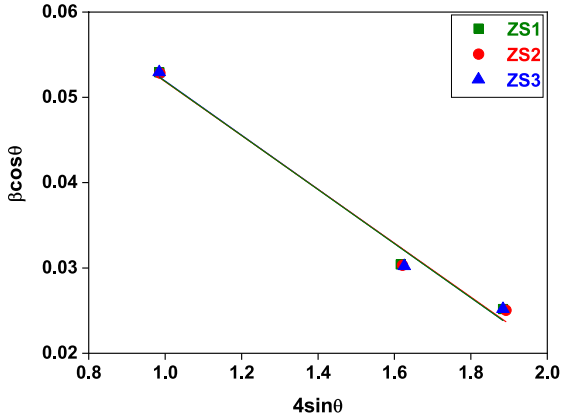

Fig. 2. W–H plot of $Zn_{1-x}Mg_xS$ (x = 0, 0.1 and 0.2) QDs.

that the bacterium culture was evenly distributed across the agar surface. To investigate the antibacterial activity of the undoped and Mg-doped ZnS QDs, disc-shaped filter paper soaked with different QD dosages (30, 40, and 50 mg/ml) were created one at a time and placed onto separate plates. As a control, erythromycin, a widely accepted antibiotic, was used as a reference medication. The discs soaked with erythromycin were also placed on the agar plates. Following that, the prepared petri plates underwent an incubation period of 24 h at a temperature of 37 °C. Throughout this duration, the antibacterial attributes of both undoped and Mg-doped ZnS QDs, along with erythromycin, engaged in interactions with the bacterial cultures. As a result, zones of inhibition, indicating the areas where bacterial growth was inhibited, formed around the discs. After the incubation period, the zones of inhibition produced by each QD and erythromycin disc were measured using a millimeter scale. The diameter of each zone represented the effectiveness of the antibacterial agent against the respective bacterium culture. By measuring these zones, the inhibitory effect and concentration of each QD were determined and compared.

3. Results and discussion

3.1. Structural analysis

The X-ray diffraction (XRD) patterns depicted in Fig. 1 were employed to evaluate the structural properties of both undoped and Mg-doped ZnS QDs. This analysis allowed for a comprehensive assessment of their respective characteristics. The QDs exhibited diffraction peaks that corresponded to a cubic blende structure of ZnS. This finding was consistent with the information provided in the JCPDS card, No. 05–0566, thereby establishing a favourable agreement [29]. No secondary phases associated with magnesium, such as colloidal magnesium or MgS, were observed. This absence indicated the exclusive presence of the ZnS crystalline phase. To determine the average crystallite size of the QDs, Debye-Scherrer's equation was utilized for calculation purposes [30],

$$\text{Average crystallite size (D)} = \frac{0.9\,\lambda}{\beta\cos\theta} \quad (1)$$

The provided expression involves different parameters: θ represents the Bragg's diffraction angle, β signifies the full width at half maximum (FWHM) of the primary diffraction peak, and λ represents the X-ray wavelength (1.5406 Å).

Table 1 provides information on the peak position (2θ), FWHM (β), inter-planer spacing (d), lattice parameter (a), volume (V), and average crystallite size (D) of the $Zn_{1-x}Mg_xS$ (x = 0, 0.1, and 0.2 QDs. The data clearly indicate that the structural parameters of the ZnS QDs were not affected by Mg doping. The addition of Mg did not significantly alter the rate of ZnS growth, resulting in no significant change in the average crystallite size [30]. This observation is reinforced by the W–H plot depicted in Fig. 2, where the intercept and slope values remained unchanged with the dopant. The micro-strain of the QDs was measured to be 31.74×10^{-3}, while the D value, derived from the intercept, was determined to be 1.7 nm. Based on this analysis, we conclude that the substitution of the small ionic radii of Mg^{2+} (0.72 Å) in place of the larger ionic radii of Zn^{2+} (0.74 Å) is easily accommodated within the structure of the QDs [13,31].

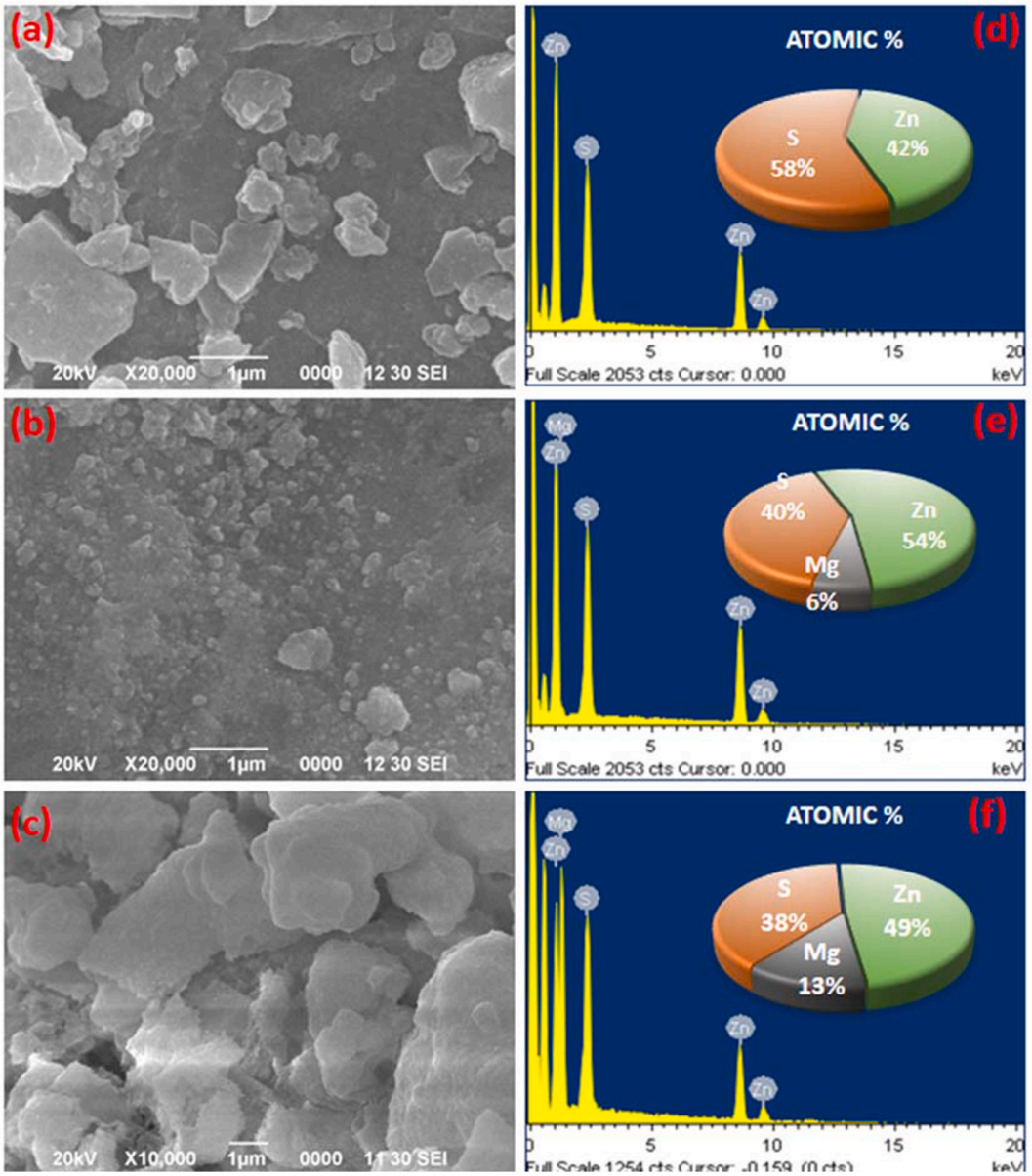

Fig. 3. SEM images of a) ZnS b) $Zn_{0.9}Mg_{0.1}S$ and c) $Zn_{0.8}Mg_{0.2}S$ QDs, respectively, and the Energy dispersive X-ray (EDX) spectra of d) ZnS e) $Zn_{0.9}Mg_{0.1}S$ f) $Zn_{0.8}Mg_{0.2}S$ QDs respectively.

The small difference in ionic radii between the host Zn^{2+} and dopant Mg^{2+} (approximately 0.02 Å) does not significantly impact the structural parameters. Additionally, the lattice parameters remain unchanged with varying Mg dopant concentrations due to the higher solubility of Mg [32].

3.2. Compositional and morphological analysis

Fig. 3a–c displays the SEM images of pure and Mg doped ZnS QDs. These images depict an uneven distribution of grains within the cluster shape. As the size of nanoparticles decreases, agglomeration becomes a prominent characteristic. van der Waals forces can act between nanoparticles, leading to their aggregation. As nanoparticles get closer to each other, the van der Waals forces become stronger, causing the particles to stick together and form agglomerates. To validate the proposed composition, the EDAX spectra presented in Fig. 3d–f were employed, thereby confirming the presence of Zn, S, and Mg ions in the synthesized QDs. The rising atomic percentage of Mg indicates the proper substitution of Mg^{2+} ions into the lattice positions of Zn^{2+}. The lack of additional elements observed in the spectra serves as confirmation of the samples' purity. However, all samples exhibit a slight sulfur deficiency that

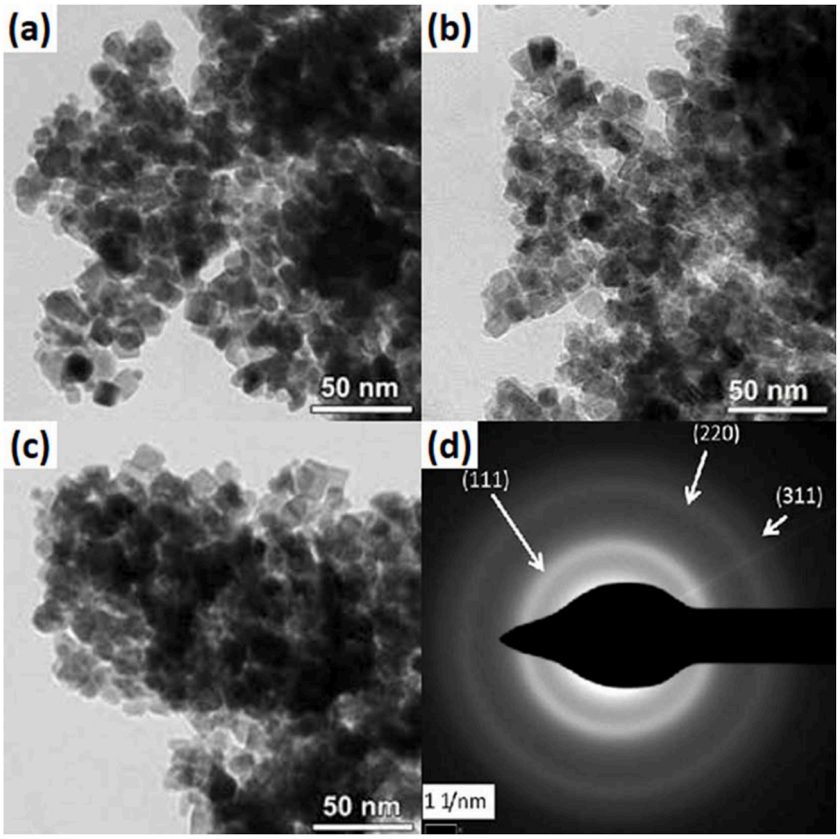

Fig. 4. TEM images of a) ZnS b) $Zn_{0.9}Mg_{0.1}S$ and c) $Zn_{0.8}Mg_{0.2}S$ QDs, respectively and d) SAED Pattern of ZnS.

becomes more pronounced with increasing concentrations of Mg doping. For Mg doping levels of 10% and 20% in ZnS, the EDAX analysis determined Mg quantities of 6.16% and 12.88%, respectively.

The size and shape of the synthesized QDs were further analyzed using transmission electron microscope (TEM), as illustrated in Fig. 4a-c. These TEM images align closely with the XRD results. Fig. 4d shows the selected area electron diffraction (SAED) pattern of ZnS, providing additional information about the crystal structure.

3.3. XPS study

The X-ray photoelectron spectroscopy (XPS) is a widely utilized technique for the analysis of surface chemistry of the synthesized QDs and bonding structure of the materials. To calibrate the binding energy scale in this study, the C 1s peak located at 285.6 eV, which corresponds to *C*–C/C–H bonds of AdC (adventitious carbon), was utilized as the reference. X-ray photoelectron spectroscopy (XPS) involves the examination of the oxidation states and chemical composition of elements by analyzing the photoelectrons emitted from the pelletized sample when exposed to X-ray irradiation. Fig. 5a displays the survey spectra of the Mg-doped ZnS QDs, providing an overview of the elemental composition. The core level spectra of Zn is shown in Fig. 5b. The prominent peaks detected at energy values of 1020.9 eV and 1044.5 eV correspond to the binding energies of Zn 2p3/2 and 2p1/2, respectively, exhibiting a spin-orbit splitting energy of 23.6 eV. The peak positions and spin-orbit splitting energy of Zn 2p3/2 and 2p1/2 in all examined samples closely align with the established literature values for ZnO, providing evidence of Zn's 2+ oxidation states [28,33,34]. The substitution of Mg induces a shift in the peaks towards lower binding energy, confirming the incorporation of Mg dopants into the Zn–S structure. Additionally, a peak corresponding to Mg 2p is observed at 49.9 (Fig. 5c) [28,35]. In Fig. 5d, the sulfur core level spectrum exhibits two peaks at energy values of 162.9 eV and 161.7 eV for S 2p3/2 and S 2p1/2, respectively. These findings closely match the literature results, providing further confirmation [28,36]. The intensity of the peak corresponding to sulfur decreases with the presence of transition metal (TM) dopants, consistent with the EDAX (energy-dispersive X-ray spectroscopy) results.

3.4. Optical study

Fig. 6a presents the optical absorption spectra of pure and Mg:ZnS QDs at room temperature. The optical absorption of the QDs demonstrates an increase with the rise in Mg dopant concentration, accompanied by a shift of the absorption peak towards higher wavelengths. Furthermore, with an increase of Mg doping concentration, the absorption peak exhibits broadening. The absorption

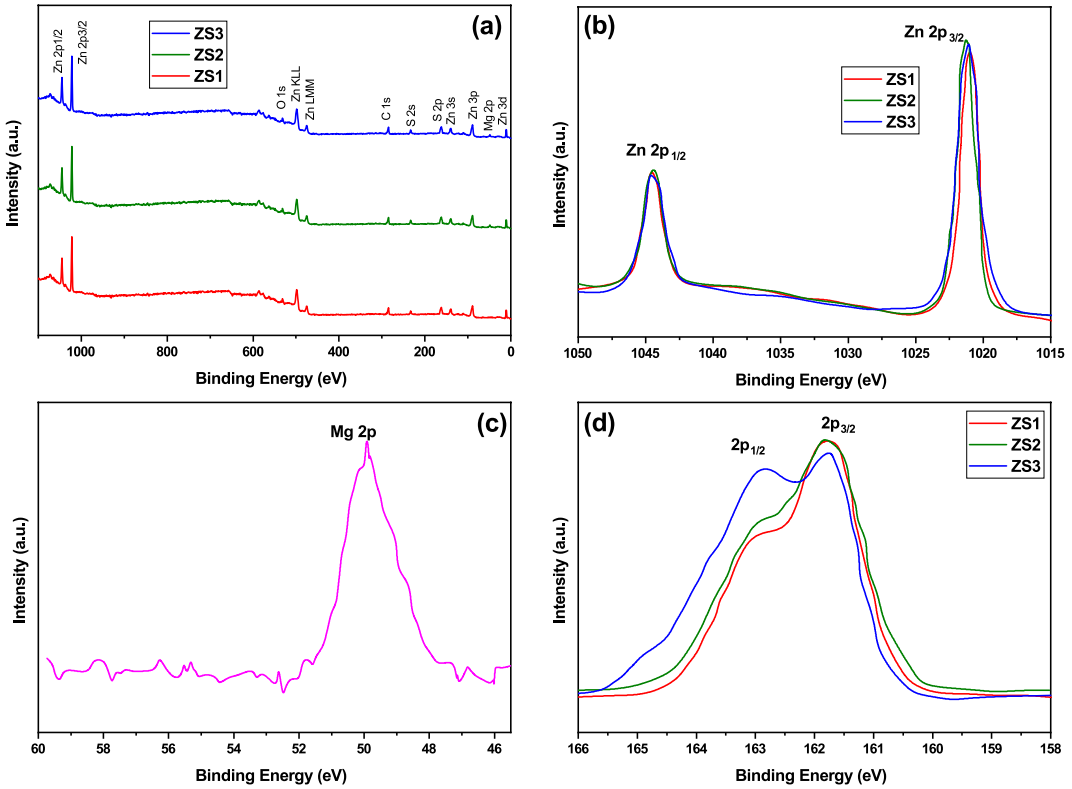

Fig. 5. a) XPS Survey spectra of Mg doped ZnS QDs and core level spectra of b) Zn 2p b) Mg 2p and c) S 2p .

characteristics of nanomaterials are influenced by several factors, including carrier density, defect states, band gap, and the electronegativity of dopant, among others. The observed rise in absorption, attributed to the addition of Mg dopant, can be attributed to two factors: the heightened carrier concentration and the introduction of defect sites caused by the presence of Mg dopant [32]. The notable enhancement in optical absorption indicates that the substitution of high electronegative Zn (1.6) with low electronegative Mg (1.2) promotes the generation of photo-induced electron-hole pairs [37].

To calculate the optical band gap, Tauc's relation, represented by Equation (2), is utilized:

$$h\upsilon = A(h\upsilon - E_g)^n \quad (2)$$

Here, A represents a constant, Eg represents band gap, and the exponent n depends transition type. In this study, Tauc plot was employed to determine the band gaps (Eg) of the QDs. The estimation of the band gap value involved extending the linear portion of the curve towards the energy axis, as demonstrated in Fig. 6b. The values of band gap for ZnS QDs doped with 0%, 10%, and 20% Mg were found to be 3.94 eV, 3.86 eV, and 3.72 eV, respectively.

The band gap of the semiconductor nanoparticles is typically influenced by two key factors: the compositional effects and the quantum confinement effects [38]. In the case of the Mg-doped ZnS QDs, where the average crystallite size does not exhibit significant changes, the reduction in band gap with increasing Mg dopant concentration is primarily attributed to the compositional effect. According to theoretical calculations conducted by Bhandari et al. band gap of the MgS was predicted to be 3.278 eV using Density Functional Theory (DFT) calculations [39]. However, experimental results indicated that the band gap of MgS-based thin films fell within the range of 3.54 eV [40]. Considering that the band gap of MgS is lower than that of ZnS (3.68 eV), the substitution of Mg leads to a reduction in the band gap of the ZnS QDs.

3.5. *Photoluminescence study*

Fig. 7 displays the photoluminescence spectra of pure and Mg:ZnS QDs. The emissions exhibited a broad range, covering wavelengths from UV to green regions. The broad emission spectrum observed in the nanocrystals is a result of the significant variation in their sizes, leading to an overlap between the band-edge emission and trap-state emission peaks. Additionally, the intensity patterns of the emitted light exhibit a crisscross layout, alternating between high and low values. This behavior can be attributed to two factors: firstly, variations in the number of nanocrystals of different sizes, and secondly, structural reasons such as the density of defects within the nanocrystals. To deconvolute the peaks, Gaussian fitting was employed to analyze the emission curves. The deconvolution process revealed five distinct emissions in the UV, violet, blue, and green regions. The weak UV emissions at 340 nm can be ascribed to the near

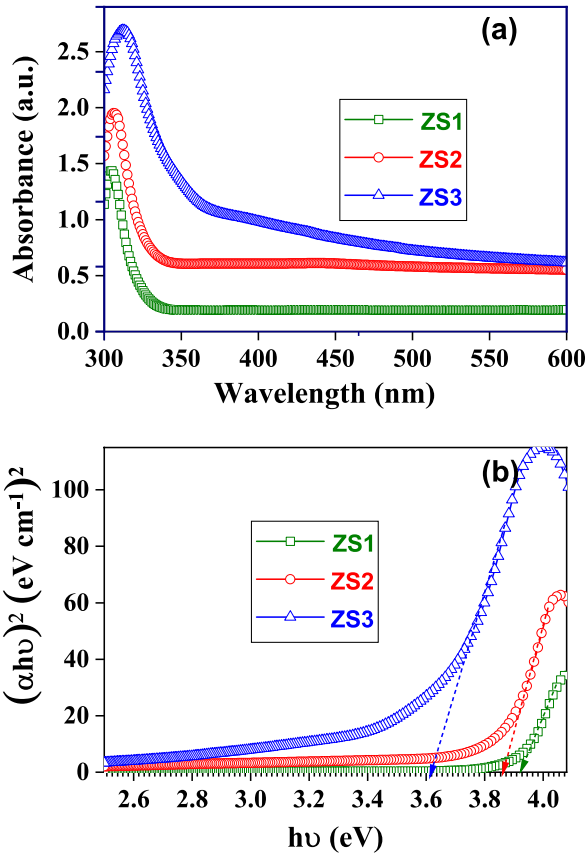

Fig. 6. a)UV–Visible absorption spectra and b) Tauc's plot of $Zn_{1-x}Mg_xS$ (x = 0, 0.1 and 0.2) QDs at room temperature.

band edge (NBE) emission of free excitons in the conduction band [41]. As the concentration of Mg dopant increases, the UV emission peak shifts towards longer wavelengths, which is consistent with the reduction in band gap observed in the UV absorption studies. This shift is a result of the band gap reduction caused by the presence of Mg dopants.

The deep donor level (Zni), situated just below the conduction band, has a longer lifetime compared to the conduction band. The conduction band electrons relax to the deep donor level (Zni) and then recombine with holes near the top of the valence band, resulting in an emission with a slightly longer wavelength than the UV emission (382 nm) [40]. The transition between shallow donor and acceptor levels (Zni) gives rise to the green emissions observed at 517 nm [41]. Additionally, violet and blue emissions at 428 nm and 479 nm, respectively, are caused by sulfur-related point defects in the ZnS lattice [13]. The emission centered at 428 nm corresponding to the transition of electron from conduction band interstitial sulfur and emission at 479 nm attributed to recombination at sulfur vacancy sites [42]. The spectra indicate that the luminescence is significantly enhanced with 10% Mg doping, while further increases in Mg concentration do not show a significant increase in luminescence intensity.

3.6. Photocatalytic activity

The photocatalytic efficiency of the Mg doped ZnS QDs have been studied with methylene blue (MB) dye solution under different time intervals from 0 to 90 min. The photocatalytic activity of the QDs has been studied by measuring the rate of fall in absorption intensities of MB dye solution. The rate of methylene blue dye degradation is calculated using the formula,

$$D\% = \frac{C0 - Ct}{C0} \times 100\% \tag{3}$$

where C_0 and C_t represent the MB dye concentrations before and after exposure to light, respectively [38,39]. Fig. 8 displays the dye degradation rate at various time intervals ranging from 0 to 90 min. The pure ZnS QDs exhibit a 90% decolorization of the MB dye solution within 90 min. However, the Mg:ZnS QDs demonstrate a higher degradation rate compared to pure ZnS. Specifically, the 10% Mg:ZnS QDs rapidly decolorize the solution, achieving 90% decolorization in just 40 min. The complete decolorization of the MB dye solution (~100%) is achieved at approximately 70 min. In general, the observed photocatalytic activity can be attributed to the generation of photo-induced reactive oxygen species (ROS) such as hydroxyl radicals, hydrogen peroxide, and superoxide anions [40].

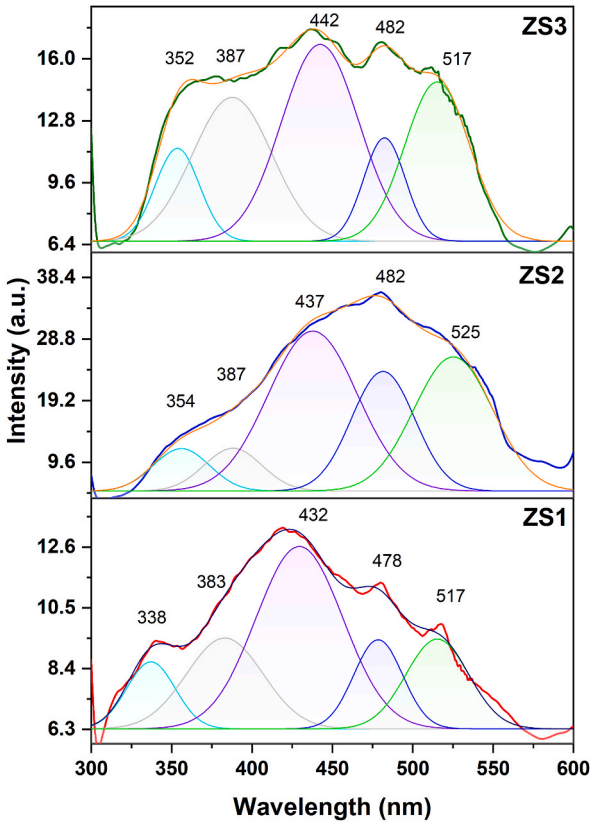

Fig. 7. Photoluminescence (PL) spectra of $Zn_{1-x}Mg_xS$ (x = 0, 0.1 and 0.2) QDs at room temperature.

The improved optical absorption of Mg:ZnS QDs facilitates the production of electron-hole pairs, thereby enhancing the photocatalytic activity. The photo-generated electron-hole pairs decolorize the dye via ROS as follows [40,43],

$$ZnS + h\vartheta \rightarrow ZnS^* + e^- + h^+$$

$$H_2O + h^+ \rightarrow OH^* + H^+$$

$$O_2 + e^- \rightarrow O^{2-*}$$

$$O^{2-} + H^+ \rightarrow HO_2^*$$

$$2HO_2^* \rightarrow H_2O_2 + O_2$$

$$H_2O_2 \rightarrow 2OH^-$$

$$OH^- + Dye \rightarrow CO_2 + H_2O$$

The increase in Mg doping concentration from 10% to 20% significantly decreases the photocatalytic activity [44]. A strong correlation found between the photocatalytic activity and NBE in PL spectra reported in the earlier literature [23,45]. The decline in the NBE emission shows its less recombination efficiency; hence, these photo-generated charge carriers increases the ROS generation which responsible for degradation of dye [23]. Therefore, the high degradation rate of 10% of Mg doped ZnS QDs is because of its less NBE. The increase in NBE emission at a higher doping percentage weakens the photocatalytic activity of the QDs. Nouri et al. noticed a similar decrease in photocatlytic activity of Mg-doped ZnO nanoparticles at Mg = 20% [46]. The reuse of the 10% of Mg doped ZnS QDs to decolorize the MB dye is shown in Fig. 8b. The photocatalytic efficiency of the dye is decrease in small amount in every reuse due to the loss during recollection process. The used catalyst is still have high activity even after reused up to 5 times.

Fig. 9 depicts the assessment of different reactive oxygen species (ROS), including OH* and O_2^-, along with photo generated charges (electrons and holes), in the mechanism of decolorization of MB dye. To analyze the individual contributions of O_2^-, OH*, electrons, and holes, scavenging agents including ascorbic acid (AA), potassium bicarbonate ($KHCO_3$), potassium sulfate (K_2SO_4), and potassium chloride (KCl) were utilized in conjunction with 10% Mg-doped ZnS [28,47]. In the absence of any scavenging agent, a remarkable degradation efficiency of approximately 96.9% for the MB dye was achieved within 60 min, indicating a high efficiency of degradation.

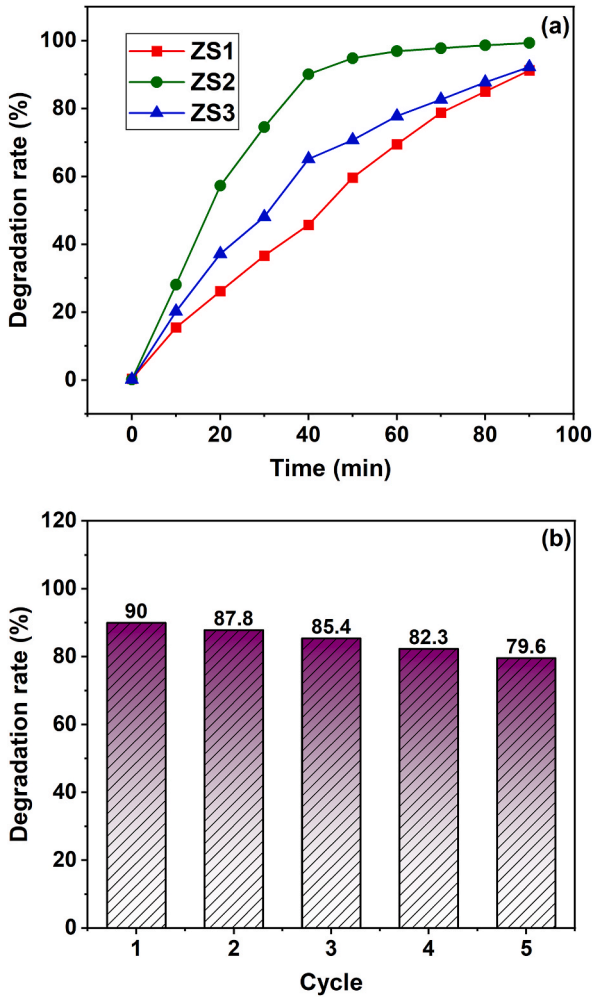

Fig. 8. Photocatalytic efficiency of $Zn_{1-x}Mg_xS$ (x = 0, 0.1 and 0.2) QDs on methylene blue (MB) dye.

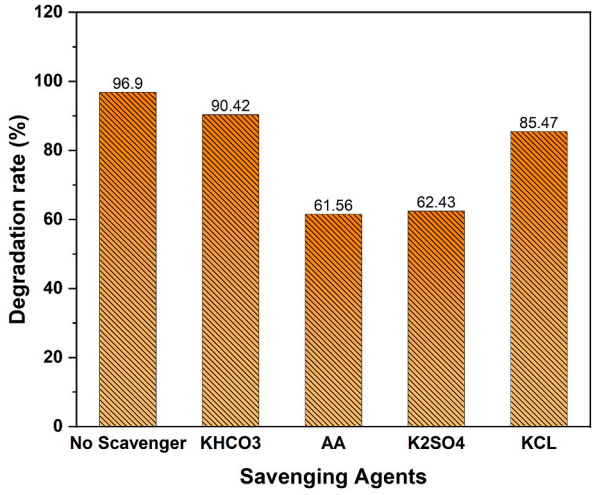

Fig. 9. The effect of savaging agents on the photocatalytic activity of $Zn_{0.9}Mg_{0.1}S$ QDs on methylene blue (MB) dye.

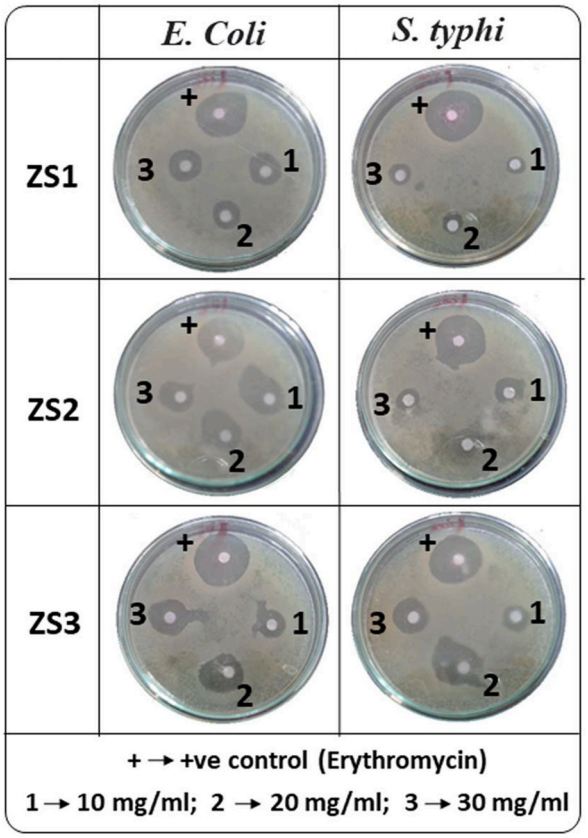

Fig. 10. Antibacterial activity of $Zn_{1-x}Mg_xS$ (x = 0, 0.1 and 0.2) QDs against *Escherisia coli* and *Salmonella typhi* bacteria.

However, when AA and K_2SO_4 were present, the degradation rate decreased by approximately 41%. This suggests that O_2^- and e^- play a dominant role in the photodegradation process of the MB dye when QDs are present. Conversely, the presence of KCl and $KHCO_3$ resulted in a decrease in degradation efficiency by 17% and 12% respectively, indicating a minor removal efficiency of OH* and photogenerated holes. These results suggest that various reactive oxygen species (ROS), as well as photogenerated electrons and holes, contribute to the effective removal of the MB dye. These findings align with previous studies conducted on similar systems [28,47,48].

3.7. Antibacterial activity

The antibacterial efficiency of pure and Mg:ZnS QDs against gram-negative *E. Coli* and *S. typhi* bacterial strains was examined using the agar disk diffusion method (Fig. 10). The zone of inhibition (ZOI) for pure ZnS and Mg:ZnS QDs at various dosages is shown in Fig. 11. Mg:ZnS QDs exhibited significant antibacterial potential against *E. Coli* (Fig. 11a), which is responsible for 75–95% of urinary tract infections, and the ZOI increased with the dopant concentration. At a concentration of 30 mg/ml, the 20% Mg:ZnS QDs showed a maximum ZOI of 24 mm. Conversely, the antibacterial activity against *S. typhi*, the bacteria that causes typhoid fever, increased initially with the dopant concentration and then remained constant or declined at higher concentrations (Fig. 11b). The maximum ZOI against *S. typhi* was observed for the 10% Mg:ZnS QDs at a concentration of 30 mg/ml. The internalization of nanomaterials and the release of Zn^{2+} ions generally result in cell damage in pathogenic bacterial strains [33,37,49]. Due to their smaller size (about 200 times smaller than the bacteria) and larger surface area, Mg:ZnS QDs exhibit increased internalization and electrostatic attraction to the cell membrane. As a result, the QDs inhibit the growth of pathogenic bacterial strains in their vicinity. Additionally, the antibacterial activity of Mg:ZnS QDs against *E. Coli* and *S. typhi* bacterial strains is enhanced by the reactive oxygen species (ROS) generated by photo-induced electron and hole pairs [49].

3.8. Conclusion

The undoped and Mg doped ZnS QDs were synthesized using the co-precipitation method, successfully incorporating the smaller Mg^{2+} ions into the Zn^{2+} lattice positions without causing any significant changes to the structural parameters. Photoluminescence (PL) emission analysis revealed the presence of various emissions, including NBE emission associated with UV radiation, as well as violet, blue, and green emissions corresponding to sulfur vacancies and Zn defects. Furthermore, the photocatalytic degradation of MB dye

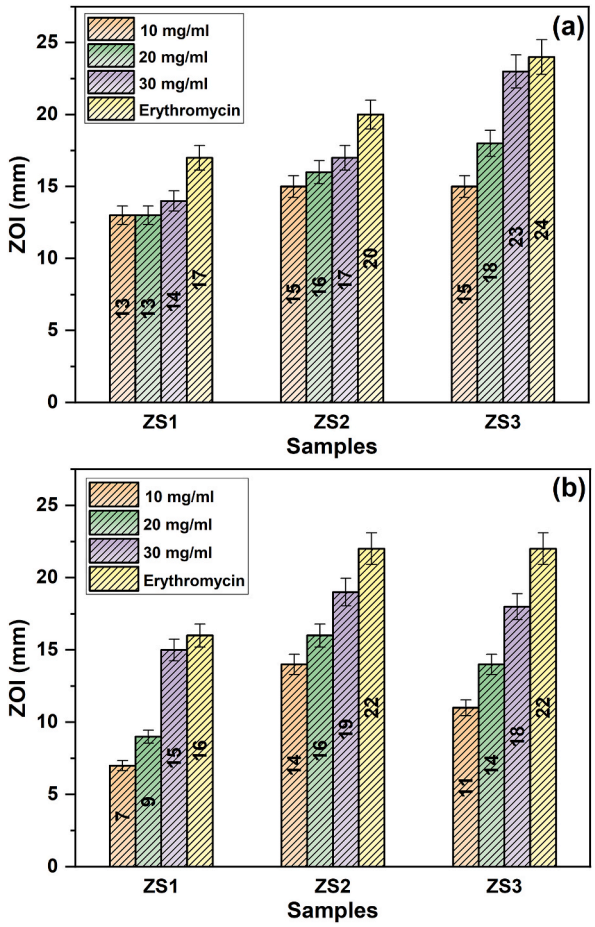

Fig. 11. Zone of inhibition (ZOI) of QDs against a) *Escherisia coli* and b) *Salmonella typhi* bacteria.

was investigated, and the presence of Mg dopant led to an improvement in photocatalytic efficiency. Among the different dopant concentrations, the 10% Mg:ZnS QDs exhibited the highest photocatalytic efficiency, demonstrating rapid decolorization of the dye. This enhancement can be attributed to the reduced electron-hole recombination rate facilitated by the Mg dopant, thereby promoting enhanced photocatalytic activity. Moreover, the antibacterial activity of Mg:ZnS QDs against *E. Coli* and *S.typhi* bacterial strains was found to be superior. This observation suggests the potential of Mg:ZnS QDs as an effective candidate material for various wastewater treatment applications, including dye degradation and antibacterial efficiency.

Author contribution statement

S. Murugan: Performed the experiments; Wrote the paper.
M. Ashokkumar: Conceived and designed the experiments; Analyzed and interpreted the data; Wrote the paper.
P. Sakthivel, Dongjin Choi: Contributed reagents, materials, analysis tools or data.

Data availability statement

Data will be made available on request.

Declaration of competing interest

The authors declare that they have no known competing financial interests or personal relationships that could have appeared to influence the work reported in this paper.

Acknowledgment

This work was supported by the International Science & Business Belt support program, through the Korea Innovation Foundation

funded by the Ministry of Science and ICT(No:2023-SB-SB-0105-01-101)

References

[1] A. Samadi-Maybodi, H. Farzinia, Application of CdS QDs incorporated in magnetized powder activated carbon for degradation of some dyes: photodegradation process and comprehensive catalytic and spectroscopic studies, J. Photochem. Photobiol. Chem. 357 (2018) 103–117, https://doi.org/10.1016/j.jphotochem.2018.01.019.

[2] W.A.A. Mohamed, I.A. Ibrahem, A.M. El-Sayed, H.R. Galal, H. Handal, H.A. Mousa, A.A. Labib, Zinc oxide quantum dots for textile dyes and real industrial wastewater treatment: solar photocatalytic activity, photoluminescence properties and recycling process, Adv. Powder Technol. 31 (2020) 2555–2565, https://doi.org/10.1016/j.apt.2020.04.017.

[3] S. Dong, J. Feng, M. Fan, Y. Pi, L. Hu, X. Han, M. Liu, J. Sun, J. Sun, Recent developments in heterogeneous photocatalytic water treatment using visible light-responsive photocatalysts: a review, RSC Adv. 5 (2015) 14610–14630, https://doi.org/10.1039/c4ra13734e.

[4] C. Chen, W. Bi, Z. Xia, W. Yuan, L. Li, Hydrothermal synthesis of the CuWO4/ZnO composites with enhanced photocatalytic performance, ACS Omega 5 (2020) 13185–13195, https://doi.org/10.1021/acsomega.0c01220.

[5] G. Mamba, A.K. Mishra, Graphitic carbon nitride (g-C3N4) nanocomposites: a new and exciting generation of visible light driven photocatalysts for environmental pollution remediation, Appl. Catal., B 198 (2016) 347–377, https://doi.org/10.1016/j.apcatb.2016.05.052.

[6] S. Banerjee, S.C. Pillai, P. Falaras, K.E. O'shea, J.A. Byrne, D.D. Dionysiou, New insights into the mechanism of visible light photocatalysis, J. Phys. Chem. Lett. 5 (2014) 2543–2554, https://doi.org/10.1021/jz501030x.

[7] A.R. Santos, A.S. Miguel, L. Tomaz, R. Malhó, C. Maycock, M.C. Vaz Patto, P. Fevereiro, A. Oliva, The impact of CdSe/ZnS Quantum Dots in cells of Medicago sativa in suspension culture, J. Nanobiotechnol. 8 (2010) 1–14, https://doi.org/10.1186/1477-3155-8-24.

[8] D. Zhu, Q. Zhou, Action and mechanism of semiconductor photocatalysis on degradation of organic pollutants in water treatment: a review, Environ. Nanotechnol. Monit. Manag. 12 (2019), 100255, https://doi.org/10.1016/j.enmm.2019.100255.

[9] C. Venkata Reddy, N. Bandaru, J. Shim, S.V.P. Vattikuti, Synthesis of CdO/ZnS heterojunction for photodegradation of organic dye molecules, Appl. Phys. Mater. Sci. Process 123 (2017) 1–12, https://doi.org/10.1007/s00339-017-1013-3.

[10] M. Muruganandham, I.S. Chen, J.J. Wu, Effect of temperature on the formation of macroporous ZnO bundles and its application in photocatalysis, J. Hazard Mater. 172 (2009) 700–706, https://doi.org/10.1016/j.jhazmat.2009.07.053.

[11] M. Muruganandham, J.J. Wu, Synthesis, characterization and catalytic activity of easily recyclable zinc oxide nanobundles, Appl. Catal., B 80 (2008) 32–41, https://doi.org/10.1016/j.apcatb.2007.11.006.

[12] E. Yassitepe, H.C. Yatmaz, C. Ozturk, K. Ozturk, C. Duran, Photocatalytic efficiency of ZnO plates in degradation of azo dye solutions, J. Photochem. Photobiol. Chem. 198 (2008) 1–6, https://doi.org/10.1016/j.jphotochem.2008.02.007.

[13] M. Ashokkumar, A. Boopathyraja, Structural and optical properties of Mg doped ZnS quantum dots and biological applications, Superlattice. Microst. 113 (2018) 236–243, https://doi.org/10.1016/j.spmi.2017.11.005.

[14] E.B. Manaia, R.C.K. Kaminski, B.L. Caetano, M. Magnani, F. Meneau, A. Rochet, C.V. Santilli, V. Briois, C. Bourgaux, L.A. Chiavacci, The critical role of thioacetamide concentration in the formation of ZnO/ZnS heterostructures by sol-gel process, Nanomaterials 8 (2018) 1–15, https://doi.org/10.3390/nano8020055.

[15] S. Muthu Kumaran, M. Ashok Kumar, Size dependent structural, optical and morphological properties of ZnS:Cu thin films, J. Mater. Sci. Mater. Electron. 23 (2012) 811–815, https://doi.org/10.1007/s10854-011-0497-4.

[16] X. Wang, H. Huang, B. Liang, Z. Liu, D. Chen, G. Shen, ZnS nanostructures: synthesis, properties, and applications, Crit. Rev. Solid State Mater. Sci. 38 (2013) 57–90, https://doi.org/10.1080/10408436.2012.736887.

[17] S. Xiong, B. Xi, C. Wang, D. Xu, X. Feng, Z. Zhu, Y. Qian, Tunable synthesis of various wurtzite ZnS architectural structures and their photocatalytic properties, Adv. Funct. Mater. 17 (2007) 2728–2738, https://doi.org/10.1002/adfm.200600891.

[18] L. Shi, K. Bao, J. Cao, Y. Qian, Growth and characterization of ZnS porous nanoribbon array constructed by connected nanocrystallities, CrystEngComm 11 (2009) 2308–2312, https://doi.org/10.1039/b909599c.

[19] M. Jothibas, M. Elayaraja, E. Paulson, S. Srinivasan, B.A. Kumar, Dynamic photocatalytic degradation of organic pollutants employing co-doped ZnS nanoparticles synthesized via solid state reaction method, Surface. Interfac. 33 (2022), 102249, https://doi.org/10.1016/j.surfin.2022.102249.

[20] G.J. Lee, J.J. Wu, Recent developments in ZnS photocatalysts from synthesis to photocatalytic applications — a review, Powder Technol. 318 (2017) 8–22, https://doi.org/10.1016/j.powtec.2017.05.022.

[21] K. Bera, S. Saha, P.C. Jana, Temperature dependent synthesis of zinc sulfide nanocrystals, Orient. J. Chem. 34 (2018) 1665–1669, https://doi.org/10.13005/ojc/340363.

[22] T. Iqbal, K. Munir, S. Afsheen, M. Zafar, M. Abrar, M.T. Qureshi, M. Al Elaimi, R.A. Hameed, R. Chand, G. Yunus, Green synthesis of Ag2S/ZnS composites and their application for seeds germination to explore critical aspect, J. Inorg. Organomet. Polym. Mater. 32 (2022) 2221–2234, https://doi.org/10.1007/S10904-022-02293-1/METRICS.

[23] R.R., V.K. Vinodkumar Etacheri, Mg-doped ZnO nanoparticles for efficient Mg-doped ZnO nanoparticles for efficient sunlight-driven, Spectrochim. Acta Mol. Biomol. Spectrosc. 130 (2014) 581–590.

[24] Ü. Ozgur, Y.I. Alivov, C. Liu, A. Teke, M.A. Reshchikov, S. Dogan, V. Avrutin, S.J. Cho, H. Morko, A comprehensive review of ZnO materials and devices, J. Appl. Phys. 98 (2005) 1–103, https://doi.org/10.1063/1.1992666.

[25] O. Dobrozhan, O. Diachenko, M. Kolesnyk, A. Stepanenko, S. Vorobiov, P. Baláž, S. Plotnikov, A. Opanasyuk, Morphological, structural and optical properties of Mg-doped ZnO nanocrystals synthesized using polyol process, Mater. Sci. Semicond. Process. 102 (2019), https://doi.org/10.1016/j.mssp.2019.104595.

[26] H.R. Rajabi, O. Khani, M. Shamsipur, V. Vatanpour, High-performance pure and Fe3+-ion doped ZnS quantum dots as green nanophotocatalysts for the removal of malachite green under UV-light irradiation, J. Hazard Mater. 250–251 (2013) 370–378, https://doi.org/10.1016/j.jhazmat.2013.02.007.

[27] P.K. Singh, P.K. Sharma, M. Kumar, R. Dutta, S. Sundaram, A.C. Pandey, Red luminescent manganese-doped zinc sulphide nanocrystals and their antibacterial study, J. Mater. Chem. B 2 (2014) 522–528, https://doi.org/10.1039/c3tb21363c.

[28] S. Murugan, P. Ashokkumar M., Sakthivel, Preparation and characterization of ZnS:MgS nanocomposites for photocatalytic and antioxidant applications, Vacuum (2023) 215, https://doi.org/10.1016/j.vacuum.2023.112256.

[29] P. Sakthivel, S. Muthukumaran, M. Ashokkumar, Structural, band gap and photoluminescence behaviour of Mn-doped ZnS quantum dots annealed under Ar atmosphere, J. Mater. Sci. Mater. Electron. 26 (2015) 1533–1542, https://doi.org/10.1007/s10854-014-2572-0.

[30] X. Wei, S. Mei, B. Yang, Z. Chen, H. Dai, Z. Hu, G. Zhang, F. Xie, W. Zhang, R. Guo, Optical and morphological properties of single-phased and dual-emissive InP/ZnS quantum dots via transition metallic and inorganic ions, Langmuir 36 (2020) 10244–10250, https://doi.org/10.1021/acs.langmuir.0c01788.

[31] N.C.S. Selvam, S. Narayanan, L.J. Kennedy, J.J. Vijaya, Pure and Mg-doped self-assembled ZnO nano-particles for the enhanced photocatalytic degradation of 4-chlorophenol, J. Environ. Sci. (China) 25 (2013) 2157–2167, https://doi.org/10.1016/S1001-0742(12)60277-0.

[32] A.N. Mallika, A. Ramachandra Reddy, K. Sowri Babu, C. Sujatha, K. Venugopal Reddy, Structural and photoluminescence properties of Mg substituted ZnO nanoparticles, Opt. Mater. 36 (2014) 879–884, https://doi.org/10.1016/j.optmat.2013.12.015.

[33] C. Muthusamy, M. Ashokkumar, A. Boopathyraja, V.V. Priya, Enhanced ferro magnetism of (Cu, Fe/Mn) dual doped ZnO nanoparticles and assessment of in-vitro cytotoxicity and antimicrobial activity for magnetically guided immunotherapy and hyperthermia applications, Vacuum 205 (2022), 111400, https://doi.org/10.1016/j.vacuum.2022.111400.

[34] M. Li, X. Wei, S. Mei, Z. Cui, Y. Fan, B. Yang, Z. Wen, Z. Xiong, L. Wang, F. Xie, W. Zhang, R. Guo, Highly luminescent copper gallium selenium based multicomponent quantum dots: formation process and tunable white-light emission, Appl. Surf. Sci. 538 (2021), https://doi.org/10.1016/j.apsusc.2020.147907.

[35] J.L. Chen, J.H. Zhu, A query on the Mg 2p binding energy of MgO, Res. Chem. Intermed. 45 (2019) 947–950, https://doi.org/10.1007/s11164-018-3654-z.
[36] L. Mao, F. Wang, J. Mao, Polar mesoporous zinc sulfide nanosheets encapsulated in reduced graphene oxide three-dimensional foams for sulfur host, Sci. Rep. 10 (2020) 5256, https://doi.org/10.1038/s41598-020-62037-4.
[37] M. Ashokkumar, C. Muthusamy, Role of ionic radii and electronegativity of co-dopants (Co, Ni and Cr) on properties of Cu doped ZnO and evaluation of In-vitro cytotoxicity, Surface. Interfac. 30 (2022), 101968, https://doi.org/10.1016/j.surfin.2022.101968.
[38] M. Ashok Kumar, S. Muthukumaran, Effect of deposition time on structural, optical and photoluminescence properties of Cd0.9Zn0.1S thin films by chemical bath deposition method, J. Mater. Sci. Mater. Electron. 24 (2013) 2858–2865, https://doi.org/10.1007/s10854-013-1183-5.
[39] U. Bhandari, C.O. Bamba, Y. Malozovsky, L.S. Franklin, D. Bagayoko, Predictions of electronic , transport , and structural properties of magnesium sulfide (MgS) in the rocksalt structure, 1773–1784, https://doi.org/10.4236/jmp.2018.99111, 2018.
[40] N. Nithya, S. Gopi, G. Bhoopathi, An amalgam of Mg-doped TiO2 nanoparticles prepared by sol–gel method for effective antimicrobial and photocatalytic activity, J. Inorg. Organomet. Polym. Mater. 31 (2021) 4594–4607, https://doi.org/10.1007/s10904-021-02076-0.
[41] L.J. Tang, G.F. Huang, Y. Tian, W.Q. Huang, M.G. Xia, C. Jiao, J.P. Long, S.Q. Zhan, Efficient ultraviolet emission of ZnS nanospheres: Co doping enhancement, Mater. Lett. 100 (2013) 237–240, https://doi.org/10.1016/j.matlet.2013.03.036.
[42] P. Hu, C. Xie, Z. Mao, X. Liang, A mechanochemical route for ZnS nanocrystals, and batch sorting along size distribution, Nanomaterials 9 (2019) 1325, https://doi.org/10.3390/NANO9091325.
[43] U. Jabeen, S.M. Shah, S.U. Khan, Photo catalytic degradation of Alizarin red S using ZnS and cadmium doped ZnS nanoparticles under unfiltered sunlight, Surface. Interfac. 6 (2017) 40–49, https://doi.org/10.1016/j.surfin.2016.11.002.
[44] M.A. Vargas, E.M. Rivera-Munoz, J.E. Diosa, E.E. Mosquera, J.E. Rodriguez-Paez, Nanoparticles of ZnO and Mg-doped ZnO: synthesis, characterization and efficient removal of methyl orange (MO) from aqueous solution, Ceram. Int. 47 (2021) 15668–15681, https://doi.org/10.1016/j.ceramint.2021.02.137.
[45] K. Pradeev raj, K. Sadaiyandi, A. Kennedy, S. Sagadevan, Z.Z. Chowdhury, M.R. Bin Johan, F.A. Aziz, R.F. Rafique, R. Thamiz Selvi, R. Rathina bala, Influence of Mg doping on ZnO nanoparticles for enhanced photocatalytic evaluation and antibacterial analysis, Nanoscale Res. Lett. 13 (2018), https://doi.org/10.1186/s11671-018-2643-x.
[46] H. Nouri, A. Habibi-Yangjeh, Microwave-Assisted method for preparation of Zn1-xMgxO nanostructures and their activities for photodegradation of methylene blue, Adv. Powder Technol. 25 (2014) 1016–1025, https://doi.org/10.1016/j.apt.2014.01.025.
[47] F. Soleimani, A. Nezamzadeh-Ejhieh, Study of the photocatalytic activity of CdS–ZnS nano-composite in the photodegradation of rifampin in aqueous solution, J. Mater. Res. Technol. 9 (2020) 16237–16251, https://doi.org/10.1016/j.jmrt.2020.11.091.
[48] W. Liu, T. He, Y. Wang, G. Ning, Z. Xu, X. Chen, X. Hu, Y. Wu, Y. Zhao, Synergistic adsorption-photocatalytic degradation effect and norfloxacin mechanism of ZnO/ZnS@BC under UV-light irradiation, Sci. Rep. 10 (2020), 11903, https://doi.org/10.1038/s41598-020-68517-x.
[49] S. Sruthi, J. Ashtami, P.V. Mohanan, Biomedical application and hidden toxicity of Zinc oxide nanoparticles, Mater. Today Chem. 10 (2018) 175–186, https://doi.org/10.1016/j.mtchem.2018.09.008.